Streaming Torque in Dust–Gas Coupled Protoplanetary Disks

Qiang Hou[1,2,3] and Cong Yu[1,2,3]

[1] School of Physics and Astronomy, Sun Yat-sen University, Zhuhai 519082, People's Republic of China; yucong@mail.sysu.edu.cn
[2] CSST Science Center for the Guangdong-Hong Kong-Macau Greater Bay Area, Zhuhai 519082, People's Republic of China
[3] State Key Laboratory of Lunar and Planetary Sciences, Macau University of Science and Technology, Macau, People's Republic of China

Abstract

We investigate the migration of low-mass protoplanets embedded in dust–gas coupled protoplanetary disks. Linear calculations are performed with respect to the Nakagawa–Sekiya–Hayashi (NSH) equilibrium within a shearing sheet. We find that the dusty quasi-drift mode dominates the dynamical behaviors in close proximity to the protoplanet. This mode exhibits an extremely short radial wavelength, characterized by a dispersion relation of $\tilde{\omega} = f_g W_s \cdot k$. The emergence of this mode leads to a wake with a short radial length scale ahead of protoplanets, contributing to a positive torque, termed as "streaming torque" (ST). Furthermore, both Lindblad torque and corotation torque are affected by the NSH velocity. The total torque and planetary migration are contingent upon the coupling strength between dust and gas. In most scenarios, ST predominates, inducing outward migration for planets, thereby addressing the issue of rapid inward migration in their formation paradigm.

1. Introduction

The interactions between planets and protoplanetary disks (PPDs) play pivotal roles in the formation and evolution of planetary systems. Planetary migration within PPDs is a natural outcome of planet–disk interaction, and three types of planetary migration have been extensively studied (Kley & Nelson 2012; Paardekooper et al. 2023). Type I migration occurs for low-mass (proto) planets (e.g., Goldreich & Tremaine 1979, 1980; Ward 1986, 1997; Korycansky & Pollack 1993; Tanaka et al. 2002; D'Angelo & Lubow 2010; Yu et al. 2010; Tanaka & Okada 2024; Wu et al. 2024; Ziampras et al. 2024). In this scenario, two components contribute: Lindblad resonance (LR) and corotation resonance. Early studies in type I migration for pure gaseous PPDs indicated rapid inward migration of planets with a timescale shorter than the lifetime of PPDs (several million years), in contradiction to both planet formation theories and observations. Additional physical ingredients such as viscosity (e.g., Yu et al. 2010), self-gravity (e.g., Pierens & Huré 2005; Baruteau & Masset 2008), magnetism (e.g., Terquem 2003; Baruteau et al. 2011), thermodynamics (e.g., Benítez-Llambay et al. 2015), and gas accretion (Laune et al. 2024; Li et al. 2024) must be considered, some of which could provide angular momentum and, in some cases, lead to outward migration. However, the lingering question of fast inward migration persists when attempting to establish a self-consistent planet formation paradigm that aligns with observations of exoplanets.

Despite its small mass fraction, dust plays a significant role in both theoretical and observational studies. However, the studies of dusty torque have been very limited due to its complexity. Some studies suggest that dust could alter migration history (Benítez-Llambay & Pessah 2018; Kanagawa 2019; Hsieh & Lin 2020; Guilera et al. 2023). Benítez-Llambay

& Pessah (2018) revealed the presence of a dust deficit behind the planet under specific conditions, resulting in a positive torque. The intricate dynamics near planets underscore the complexity of the phenomenon. This study aims to elucidate the fundamental dynamics of dust and gas and their implications for planetary migration, thereby shedding light on the underlying physics.

In this paper, we investigate planetary migration for a low-mass protoplanet embedded in dust–gas coupled PPDs. Section 2 introduces the basic equations and our methodology. Linear calculations are conducted within the framework of the Nakagawa–Sekiya–Hayashi (NSH) equilibrium under the shearing sheet approximation. Section 3 presents our findings, revealing the emergence of a dusty "quasi-drift" mode with a short wavelength, combined with "quasi-density" waves, forming a multiscale structure. We analyze their properties and morphologies. In Section 5, we calculate torques induced by these modes with various parameters, demonstrating the possibility of planetary outward migration. Finally, we offer discussions and conclusions in Section 5.

2. Basic Equations

The hydrodynamic equations for 2D dust–gas coupled thin PPDs read

$$\frac{\partial \Sigma_d}{\partial t} + \nabla \cdot (\Sigma_d \boldsymbol{V}_d) = 0, \tag{1}$$

$$\frac{\partial \Sigma_g}{\partial t} + \nabla \cdot (\Sigma_g \boldsymbol{V}_g) = 0, \tag{2}$$

$$\frac{\partial \boldsymbol{V}_d}{\partial t} + \boldsymbol{V}_d \cdot \nabla \boldsymbol{V}_d = -\nabla \Phi_\star - \frac{\boldsymbol{V}_d - \boldsymbol{V}_g}{t_s}, \tag{3}$$

$$\frac{\partial \boldsymbol{V}_g}{\partial t} + \boldsymbol{V}_g \cdot \nabla \boldsymbol{V}_g = -\nabla \Phi_\star + \frac{\Sigma_d}{\Sigma_g} \frac{\boldsymbol{V}_d - \boldsymbol{V}_g}{t_s} - \frac{\nabla P}{\Sigma_g}, \tag{4}$$

where $\boldsymbol{V}$, Σ, P, and $\Phi_\star$ are velocity, (surface) density, gas pressure, and star potential, respectively. Subscripts "d" and

"g" denote quantifies of dust and gas, respectively. t_s is the stopping time. A steady solution for these equations, known as NSH equilibrium, has been given by Nakagawa et al. (1986), i.e.,

$$V_{dr} = -f_g \chi_1 \eta V_K, \tag{5}$$

$$V_{d\theta} = (1 - f_g \chi_2 \eta) V_K, \tag{6}$$

$$V_{gr} = f_d \chi_1 \eta V_K, \tag{7}$$

$$V_{g\theta} = V_K + (f_d \chi_2 - 1) \eta V_K. \tag{8}$$

Here $f_{d/g} \equiv \Sigma_{d/g}/(\Sigma_d + \Sigma_g)$ is the mass fraction of dust–gas. $V_K(\Omega_K)$ represents the Keplerian speed (frequency). A useful dimensionless quantity can be defined as $\tau \equiv \Omega_K t_s$. Then $\chi_1 \equiv 2 f_g \tau/[1 + (f_g \tau)^2]$, $\chi_2 \equiv 1/[1 + (f_g \tau)^2]$. Moreover, $\eta \equiv -\frac{1}{2 \Sigma_g V_K^2} \frac{\partial P}{\partial \ln r} = 0.5 h^2$ quantifies the radial pressure support, with the assumptions of isothermal gas and a power–law dependency on radius for its density. h is the aspect ratio defined as $\boldsymbol{h} \equiv H/r$, where H is the scale height.

Equations (1)–(4) can be readily investigated based on the "shearing sheet" (Goldreich & Lynden-Bell 1965; Narayan et al. 1987). Linear perturbation theory is used to decompose those equations into steady and perturbation equations. A low-mass planet is embedded in the latter as a perturbation source located at the origin of the coordinate. We assume the planet is with the mass below roughly a few percent of thermal mass, M_{th}, defined by $M_{th} = h_p^3 M_\star$ ($M_\star$ is the star mass). In this regime, linear analysis behaves well (Miranda & Rafikov 2020), beyond which gap opening will occur and type II migration works. Subscript "p" denotes the values at the planet location. We adopt a Cartesian coordinate system with $x = (r - r_p)/H$ and $y = r_p(\theta - \theta_p)/H$ and neglect all curvature terms. We express perturbation quantities as integrals in Fourier space, i.e., $X_1(x, y) = \int_{-\infty}^{+\infty} \delta X(x, k_y) \exp(i k_y y) dk_y$. Lastly, we focus on the Stokes regime when dealing with drag terms, i.e., $\tau = \text{const.}$, applied when the dust size is much larger than the mean free path of the gas. It has no fundamental physical difference with the Epstein regime, when we should make $\Sigma_g \tau = \text{const.}$ (Pan & Yu 2020). Then perturbation equations for a specific k_y read

$$\left(i k_y \frac{V_{dy}}{\Omega_p} + \frac{V_{dx}}{\Omega_p} \frac{d}{dx} \right) \frac{\delta \Sigma_d}{f_d \Sigma_p} + \frac{d}{dx} \frac{\delta V_{dx}}{\Omega_p} + i k_y \frac{\delta V_{dy}}{\Omega_p} = 0, \tag{9}$$

$$\left(i k_y \frac{V_{gy}}{\Omega_p} + \frac{V_{gx}}{\Omega_p} \frac{d}{dx} \right) \frac{\delta \Sigma_g}{f_g \Sigma_p} + \frac{d}{dx} \frac{\delta V_{gx}}{\Omega_p} + i k_y \frac{\delta V_{gy}}{\Omega_p} = 0, \tag{10}$$

$$\left(\frac{1}{\tau} + i k_y \frac{V_{dy}}{\Omega_p} + \frac{V_{dx}}{\Omega_p} \frac{d}{dx} \right) \frac{\delta V_{dx}}{\Omega_p}$$
$$- \frac{2 \delta V_{dy}}{\Omega_p} - \frac{1}{\tau} \frac{\delta V_{gx}}{\Omega_p}$$
$$= -\frac{1}{c_s^2} \frac{\partial \phi_p}{\partial x}, \tag{11}$$

$$\frac{\delta V_{dx}}{2 \Omega_p} + \left(\frac{1}{\tau} + i k_y \frac{V_{dy}}{\Omega_p} + \frac{V_{dx}}{\Omega_p} \frac{d}{dx} \right) \frac{\delta V_{dy}}{\Omega_p} - \frac{1}{\tau} \frac{\delta V_{gy}}{\Omega_p} = -i k_y \frac{\phi_p}{c_s^2}$$
$$- \frac{W_{s,x}}{\tau} \frac{\delta \Sigma_d}{f_g \Sigma_p} + \left(\frac{\mu W_{s,x}}{\tau} + \frac{d}{dx} \right) \frac{\delta \Sigma_g}{f_g \Sigma_p} - \frac{\mu}{\tau} \frac{\delta V_{dx}}{\Omega_p}, \tag{12}$$

$$+ \left(\frac{\mu}{\tau} + i k_y \frac{V_{gy}}{\Omega_p} + \frac{V_{gx}}{\Omega_p} \frac{d}{dx} \right) \frac{\delta V_{gx}}{\Omega_p} - \frac{2 \delta V_{gy}}{\Omega_p} = -\frac{1}{c_s^2} \frac{\partial \phi_p}{\partial x}$$
$$- \frac{W_{s,y}}{\tau} \frac{\delta \Sigma_d}{f_g \Sigma_p} + \left(\frac{\mu W_{s,y}}{\tau} + i k_y \right) \frac{\delta \Sigma_g}{f_g \Sigma_p} - \frac{\mu}{\tau} \frac{\delta V_{dy}}{\Omega_p}, \tag{13}$$

$$+ \frac{\delta V_{gx}}{2 \Omega_p} + \left(\frac{\mu}{\tau} + i k_y \frac{V_{gy}}{\Omega_p} + \frac{V_{gx}}{\Omega_p} \frac{d}{dx} \right) \frac{\delta V_{gy}}{\Omega_p} = -i k_y \frac{\phi_p}{c_s^2}. \tag{14}$$

Here, c_s represents the sound speed. μ denotes the dust–gas ratio, f_d/f_g. $\boldsymbol{W}_s \equiv \boldsymbol{V}_d - \boldsymbol{V}_g \equiv (W_{s,x}, W_{s,y})$ denotes the relative velocity between dust and gas, and it will be called drift velocity hereafter. Moreover,

$$V_{dx} = -\frac{1}{2} f_g \chi_1 h_p \Omega_p, \tag{15}$$

$$V_{dy} = -\frac{3}{2} \Omega_p x - \frac{1}{2} f_g \chi_2 h_p \Omega_p, \tag{16}$$

$$V_{gx} = \frac{1}{2} f_d \chi_1 h_p \Omega_p, \tag{17}$$

$$V_{gy} = -\frac{3}{2} \Omega_p x + \frac{1}{2} (f_d \chi_2 - 1) h_p \Omega_p. \tag{18}$$

ϕ_p is the planet potential, expressed by Bessel functions (Goldreich & Tremaine 1980; Rafikov & Petrovich 2012), i.e.,

$$\phi_p(k_y, x) = -\frac{GM_p}{\pi H} K_0(|k_y \sqrt{x^2 + x_s^2}|), \tag{19}$$

$$\frac{\partial \phi_p}{\partial x} = \text{sgn}(x) \frac{GM_p}{\pi H} k_y K_1(|k_y \sqrt{x^2 + x_s^2}|). \tag{20}$$

K_n is the modified Bessel function of order n. x_s is the softening length, set to $1/8$, as used in Dong et al. (2011). With the above preparations, we employ the relaxation method (Press et al. 1992; Huang & Yu 2022) to solve Equations (9)–(14). This method addresses the two-point boundary value problem through an iterative process similar to the Newton–Raphson method. Equations (9)–(14) are discretized into finite-difference equations within the computational domain. Both the partial difference equations and boundary conditions (BCs) are satisfied in each iteration. We implement free outgoing BCs with the WKB approximation, similar to the approach in Li et al. (2000). To ensure sufficient convergence, we use a high resolution of $2 \times 10^{-4} H$, achieving an error less than 10^{-9}.

3. Dusty and Gaseous Modes

3.1. Wavy Behaviors

Previous studies by Squire & Hopkins (2018a, 2018b) interpreted the YG streaming instability (Youdin & Goodman 2005) as the resonance between epicyclic oscillations of gas and the drift velocity, termed as "resonant drag instability" (RDI). Furthermore, they suggest that the drift velocity can
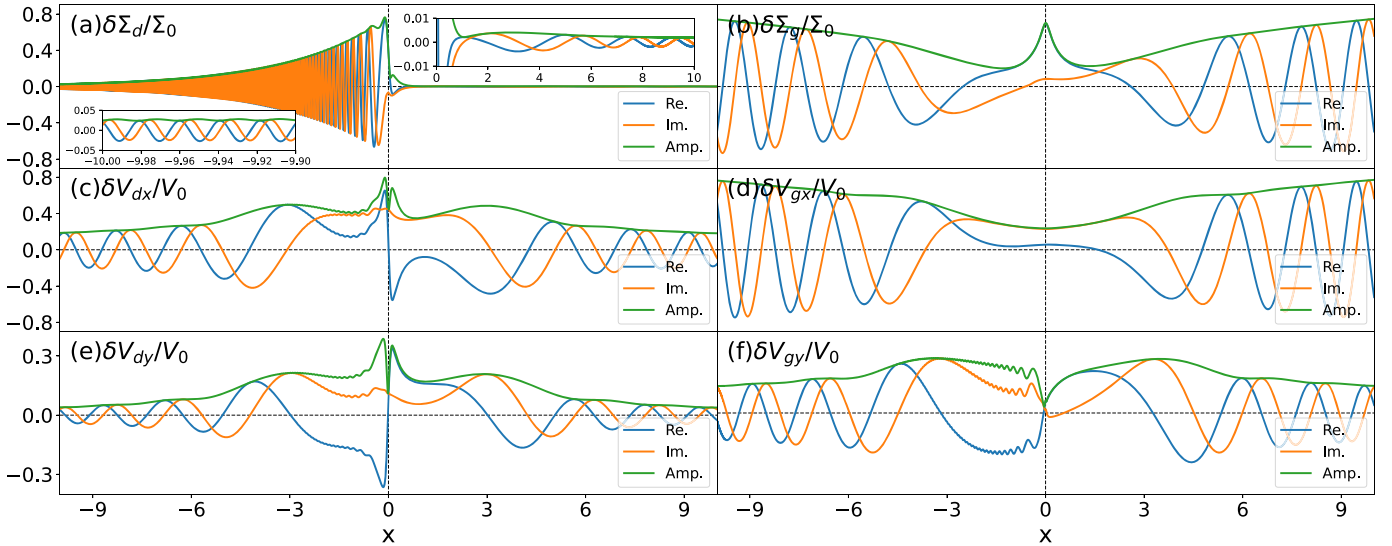
Figure 1. Dusty and gaseous waves when $f_d = 0.01$, $\tau = 1.0$, and $k_y = 0.3$. All quantities in the figure are normalized. (a) The dusty density perturbation. (b) The gaseous density perturbation. (c) The dusty radial velocity perturbation. (d) The gaseous radial velocity perturbation. (e) The dusty azimuthal velocity perturbation. (f) The gaseous azimuthal velocity perturbation.

resonate with various waves, including sound waves (Hopkins & Squire 2018). RDI occurs when the dust drift velocity exceeds the sound speed ($W_s > c_s$), leading to the emergence of instabilities. In our scenario, where $W_s \ll c_s$, RDI is absent. However, the planet can still excite certain modes.

Through solving (9)–(14) with the relaxation method, we can get as many sets of solutions as the number of k_y. For a specific case with $k_y = 0.3$, Figure 1 illustrates the excitation of dusty and gaseous waves by a planet situated at the coordinate origin. We select $f_d = 0.01$ and $\tau = 1.0$ for a clear illustration. The perturbed densities and velocities are normalized by $\Sigma_0 = q h_p^{-3} \Sigma_p$ and $V_0 = q h_p^{-3} \Omega_p$, where q represents the mass ratio of the planet to the host star ($M_p/M_\star$). In the figure, we notice that such a dust mass fraction has a minimal impact on gas, as depicted in subfigures (b), (d), and (f). The results resemble those calculated in a pure-gas disk (e.g., Tanaka et al. 2002; Rafikov & Petrovich 2012), except for the short-wavelength structure observed inside the planet. This short-wavelength structure arises due to the feedback of dust, leading us to refer to the gaseous waves as "quasi-density" waves.

Dusty perturbations exhibit distinct characteristics compared to gaseous perturbations. Subfigures (a), (c), and (e) illustrate that dusty perturbations display a short-wavelength structure inside the planet. It originates from the "quasi-drift" mode (Hopkins & Squire 2018). In the next subsection, we will solve its radial wavenumber and demonstrate that the appearance of the short-wavelength structure is robust. Identifying these features necessitates a high spatial resolution. The lower-right zoom-in panel in subfigure (a) shows that the radial wavelength near the inner boundary is about 2×10^{-2}H, which poses a significant challenge for resolution in hydrodynamic simulations. We use 2×10^{-4}H resolution, corresponding to 10^5 mesh points, to ensure that the refined structure is presented in our calculations. With such a high resolution, the solutions become converged and have no dependency on the radial domain extent or higher mesh points.

Away from the planet, dusty waves are dominated by "quasi-density" waves, except for the density perturbation inside the planet, as shown in subfigure (a). This dominance is due to the

slow damping of the quasi-drift mode and the small amplitude of the dusty quasi-density wave. The latter is depicted in the upper-right zoom-in panel, where $\delta\Sigma_d \sim f_d \delta\Sigma_g$. As f_d increases, the quasi-drift mode is damped faster, and quasi-density waves also come to dominate wavy behaviors further inside the planet. This will be further illustrated in the next subsection.

3.2. Dispersion Relation of the Quasi-drift Mode

Hopkins & Squire (2018) derived the dispersion relation for dust–gas systems in the free-falling frame. The free-drift mode exhibits a dispersion relation of $\omega = W_s \cdot k$. Similar results can be obtained in our framework. Employing WKB approximation, we numerically solve for the radial wavenumber of the quasi-drift mode. For the real part, we obtained a fitting dispersion relation of $\tilde{\omega} = f_g W_s \cdot k$. The results are depicted in Figure 2, where the upper (lower) panel displays the real (imaginary) part of the radial wavenumber k_x. In the upper row, the red solid line represents our numerical results. The blue dotted–dashed line indicates k_x of the free-drift mode, i.e., $k_x = (\tilde{\omega}_d - k_y W_{s,y})/W_{s,x}$, where $\tilde{\omega}_d$ represents the Doppler-shifted frequency of dust, defined by $k_y r(\Omega_p - \Omega_d)$. The green dotted–dashed line indicates k_x of the quasi-drift mode, i.e., $k_x = (\tilde{\omega}_d/f_g - k_y W_{s,y})/W_{s,x}$. The quasi-drift mode aligns perfectly with our numerical calculations, indicating that these short-wavelength structures arise from this mode. Furthermore, $|k_x|$ increases linearly as $|x|$ increases. Specifically, at the inner boundary ($x = -10$), $k_x \sim 300$, a value consistent with the radial wavelength of $\sim 2 \times 10^{-2}$H, as depicted in Figure 1. Lastly, both the phase velocity and group velocity of the mode are $\sim W_s$, indicating that the wave propagates inward in the $-x$ direction and ahead of the planet in the $+y$ direction.

From the lower row, we find that the quasi-drift mode is excited by the planet and propagates inward while undergoing rapid damping, particularly at locations slightly further away from the planet. This behavior is consistent with the findings of Hopkins & Squire (2018). In the absence of planets, the mode remains stable due to $W_s \ll c_s$. Consequently, its structures dominate the region near the interior of the planet, displaying asymmetry in the shearing sheet. When $f_d = 0.01$, the damping
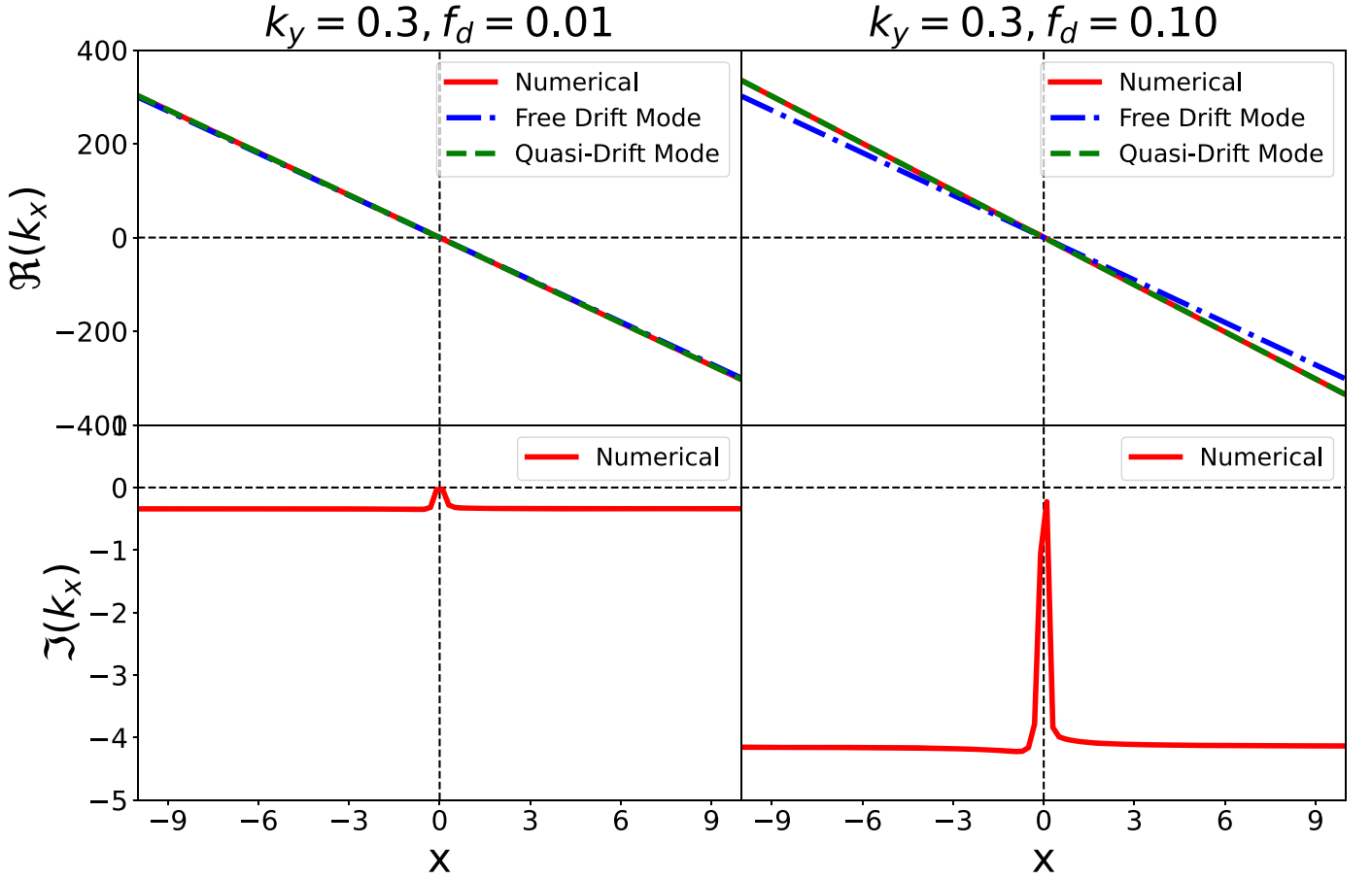
Figure 2. The radial wavenumbers of quasi-drift modes. $\tau = 1.0$ and $k_y = 0.3$, $f_d = 0.01$ and $f_d = 0.1$ are compared in two columns. The upper (lower) row represents the real (imaginary) part. Red solid lines show our numerical results. Blue dotted–dashed lines show the radial wavenumber of free-drift mode, i.e., $k_x = (\tilde{\omega}_d - k_y W_{s,y})/W_{s,x}$. Green dotted–dashed lines show the radial wavenumber of quasi-drift mode, i.e., $k_x = (\tilde{\omega}_d/f_g - k_y W_{s,y})/W_{s,x}$.
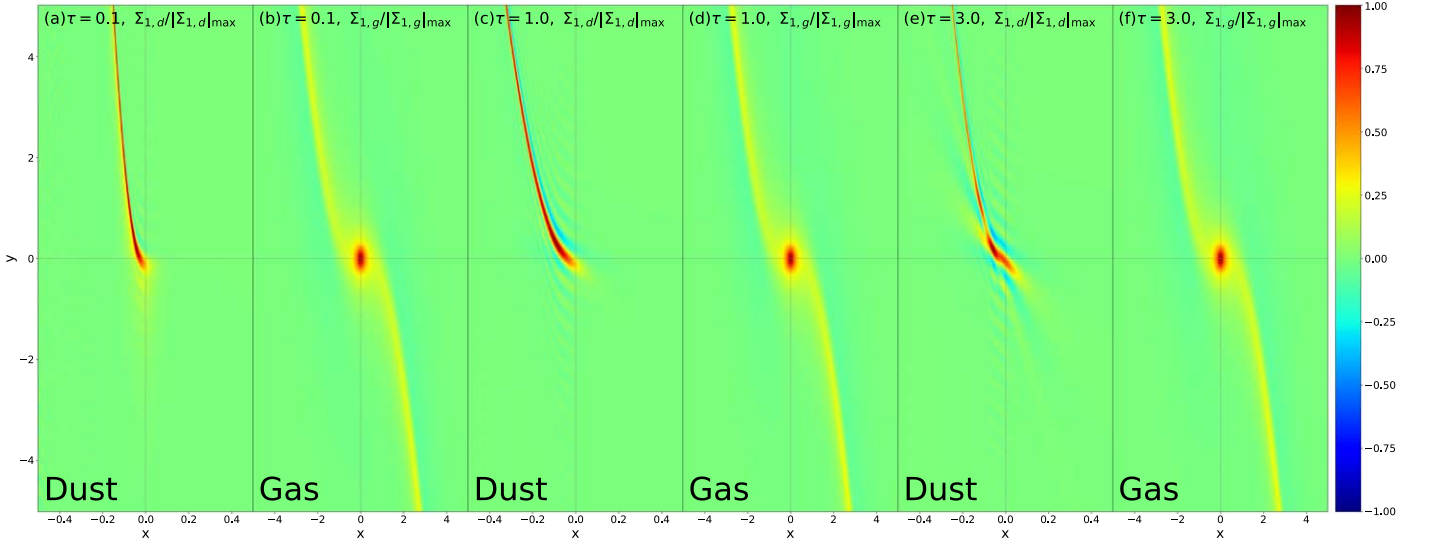

Figure 3. Planetary wakes with $f_d = 0.01$. From left to right, $\tau = 0.1$, 1.0, and 3.0, and every two panels show the dusty drift mode and gaseous density waves separately (note their ranges of x-axes are different). All perturbations in each panel are normalized by their respective maximum values.

rate is small, allowing the quasi-drift mode to dominate wavy behaviors far inside the planet. While $f_d > 0.01$, the damping rate increases rapidly away from the planet, causing quasi-density waves to dominate wavy behaviors, as illustrated in Section 4.1.

3.3. Planetary Wake

To visualize the waves in real space, we integrate density perturbations. Conclusively, the planetary wakes are depicted in Figure 3 with $f_d = 0.01$. From left to right, we consider $\tau = 0.1$, 1.0, and 3.0, with every two panels displaying the
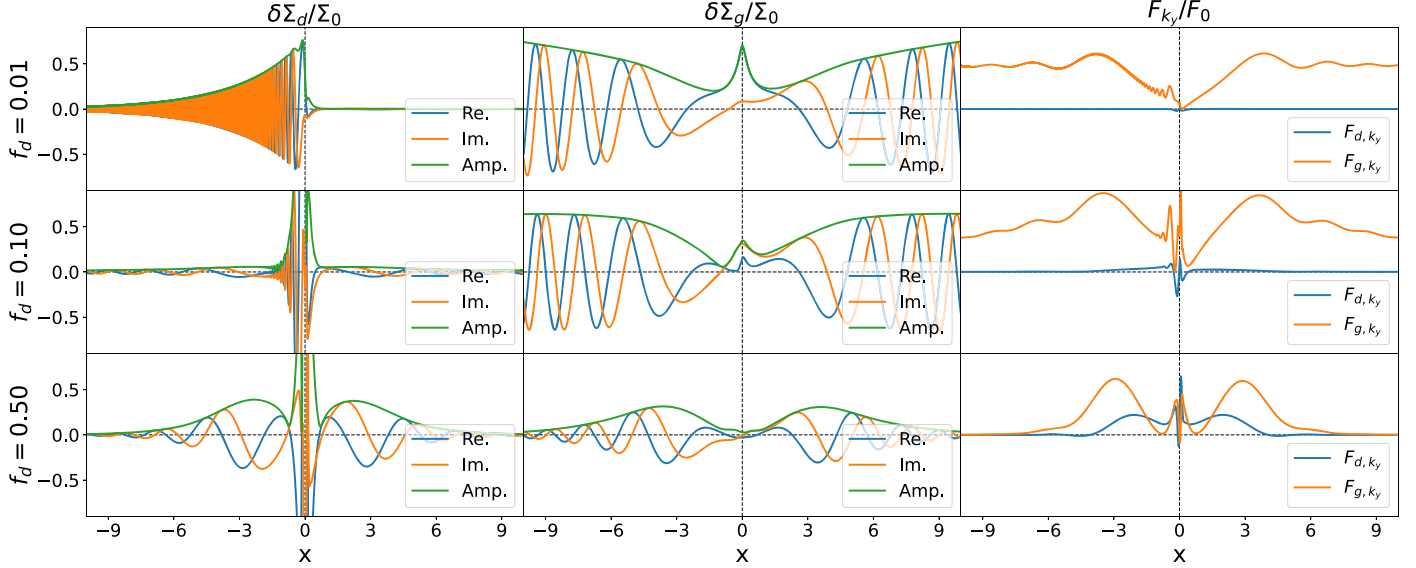
Figure 4. Dusty and gaseous density perturbations and AMFs with $\tau = 1.0$, $k_y = 0.3$, and varying f_d in each row. With f_d increasing, both dusty and gaseous AMFs diminish progressively, indicative of damped "quasi-density" waves, and the quasi-drift mode experiences heightened damping.

dusty quasi-drift mode and gaseous quasi-density waves separately (note their ranges of x-axes differ). All perturbations in each panel are normalized by their respective maximum values. Comparing panels (b), (d), and (f), we find minimal changes in gaseous quasi-density waves. However, the dusty quasi-drift mode exhibits a short radial length scale ($\sim 0.1H$). These results align with our previous analysis indicating that the quasi-drift mode is rapidly damped as it propagates inward. As aforementioned, both the phase velocity and group velocity of the mode are $\sim W_s$. Therefore, the quasi-drift mode remains ahead of the planet, exerting a positive torque on it, which is consistent with panels (a), (c), and (e). Due to the large amplitude of the mode, this effect is significant, termed as the "streaming torque" (ST). When $\tau \sim 1$, the dusty wake exhibits a larger radial extent and relative density perturbation, indicating that the torque effect is most pronounced around $\tau \sim 1$, where the drift velocity W_s reaches its maximum. Detailed calculations are presented in the subsequent section.

The morphologies of dust wave are consistent with Benítez-Llambay & Pessah (2018), who conducted hydrodynamic simulations for a dust–gas PPD. Their results present radial short-wavelength structures inside the planet, as their Figures 1 and 4 show. Dust surplus, deficit, and multiple dust gaps inside the plane might imply the nonlinear evolution phase of dusty drift mode.

4. Disk Torque and Planetary Migration

4.1. Angular Momentum Flux

For low-mass planets embedded within pure-gas PPDs, the Lindblad torque (LT), Γ_L, and corotation torque (CT), Γ_C, exerted by the disk on the planet play crucial roles in driving type I migration (Goldreich & Tremaine 1979; Ward 1986; Korycansky & Pollack 1993; Tanaka et al. 2002). These torques can be quantified by analyzing the angular momentum flux (AMF) carried by density waves, given by

$$F = \int_0^\infty F_{k_y} dk_y, \qquad (21)$$

$$F_{k_y} = 4\pi r_p^2 \Sigma_p [\mathfrak{R}(\delta V_x)\mathfrak{R}(\delta V_y) + \mathfrak{I}(\delta V_x)\mathfrak{I}(\delta V_y)]. \qquad (22)$$

Then LT and CT are given by

$$\Gamma_{L/C,k_y} = \int_0^\infty \Gamma_{L/C,k_y} dk_y, \qquad (23)$$

$$\Gamma_{L,k_y} = F_{k_y}(x \to -\infty) - F_{k_y}(x \to +\infty), \qquad (24)$$

$$\Gamma_{C,k_y} = F_{k_y}(x \to +0) - F_{k_y}(x \to -0). \qquad (25)$$

For a two-fluid system, distinct AMFs arise for dusty and gaseous waves. Figure 4 illustrates the density perturbations and AMFs for both components with $\tau = 1.0$, $k_y = 0.3$, and varying f_d. The normalization is $F_0 = q^2 h_p^{-3} \Sigma_p r_p^4 \Omega_p^2$. The first row, consistent with Figure 1, demonstrates minimal dusty AMF due to a low f_d. Gaseous AMF tends toward a constant at large distances from the planet. However, when f_d increases, as shown in subsequent rows, both dusty and gaseous AMFs diminish progressively, indicative of damped "quasi-density" waves. It means we cannot get the disk torque on planets through (21)–(25). Actually, Equation (22) does not apply in dissipation flows (Balbus 2003). In the system, dust and gas interact through friction. Then, part of kinetic energy is dissipated into heating. However, we use the isothermal state for gas. The cooling process would exert thermal damping on propagating waves. Similar behaviors appear in Miranda & Rafikov (2020) because of thermal damping. However, our current investigation focuses on low f_d and the quasi-drift mode, which exhibits substantial torques. Therefore, we do not go into detail about the damped AMFs. Notably, the quasi-drift mode experiences heightened damping as f_d increases, which is consistent with the discussion in Section 3.2. Ultimately, we refrain from utilizing Equations (21)–(25) for torque calculations. This decision stems from the inherent limitation of this method in capturing ST effects accurately.
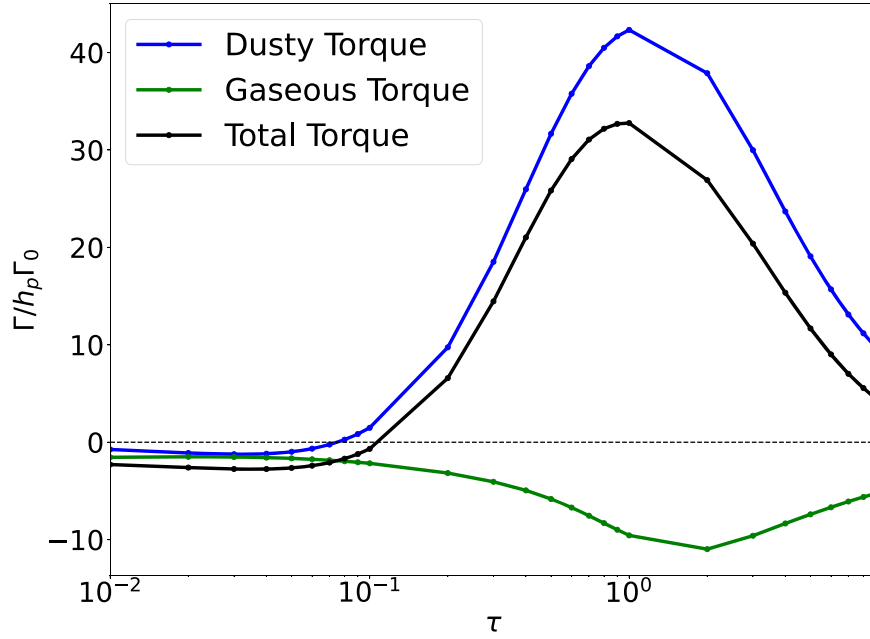
Figure 5. The disk torques on planets with $f_d = 0.01$ and different τ values. Solid dots are from our calculations, linked by three curves. The blue curve shows torques from dust modes. The green curve show those from gas modes. The black curve shows the total torque.

4.2. Torque Calculations

We can calculate the torque by integrating planetary force, which reads

$$\Gamma = r_p \int_{-\infty}^{\infty} \int_{-\infty}^{\infty} dx dy \Sigma_1 \frac{\partial \phi_p}{\partial y}. \tag{26}$$

In Fourier space,

$$\Gamma = \int_0^{\infty} \int_{-\infty}^{\infty} \left(\frac{d\Gamma}{dx}\right)_{k_y} dx dk_y, \tag{27}$$

$$\left(\frac{d\Gamma}{dx}\right)_{k_y} = -4\pi r_p k_y \phi \mathfrak{I}(\delta\Sigma). \tag{28}$$

We use Equation (27) with k_y ranging from 0.01 to 15, logarithmically discrete to 320 points. The convergence for total torques is confirmed with high spatial resolution.

The results are presented in Figure 5 for $f_d = 0.01$. The x-axis represents different τ values. The solid dots represent our calculations, linked by three curves. The blue curve indicates torques from dusty modes, labeled as "Dusty Torque," while the green curve represents those from gaseous modes, labeled as "Gaseous Torque." The black curve depicts the total torque. Here, $h_p\Gamma_0 = q^2 h_p^{-2}\Sigma_p r_p^4 \Omega_p^2$. We set $h_p = 0.03$ for comparison with Tanaka et al. (2002).

The torque analysis in Figure 5 reveals several key insights. Dusty torques predominantly exhibit positive and dominate total torques in most scenarios. Conversely, gaseous torques appear negative, driving inward migration for planets solely.

Dusty torques reach extreme points when $\tau \sim 1$, corresponding to the peak drift velocity. The dominance of dusty torques is attributed to the ST, which surpasses contributions from CT and LT for dust. Notably, when τ is sufficiently low ($\lesssim 10^{-1}$), dusty torques become negative due to strong gas–dust coupling, causing dust behavior to mimic that of gas.

The negative nature of gaseous torques aligns with their role in facilitating inward migration, a phenomenon extensively studied in prior literature (e.g., Ward 1986, 1997; Korycansky & Pollack 1993; Tanaka et al. 2002). If we consider τ to be very low or large, the gaseous torque must converge to that in a pure-gas PPD. Tanaka et al. (2002) employed the "Modified Local Approximation," which incorporates the curvature effect, surface density gradient, and pressure gradient compared to the shearing sheet. In this paper, only the effect of the pressure gradient is considered, resulting in a change of the rotation curve from Keplerian frequency. This alteration affects the locations of LR points, leading to a net LT. Our calculations yield $\Gamma_g \simeq -2.0 h_p\Gamma_0$, which is consistent with the value obtained by Tanaka et al. (2002) of $\Gamma_g \simeq -2.3 h_p\Gamma_0$, attributed solely to the pressure gradient. When $\tau \sim 1$, the gaseous radial velocity amplifies CT, leading to maximum negative gaseous torque. This phenomenon is reminiscent of type III migration, originating from planetary migration (Masset & Papaloizou 2003; Ogilvie & Lubow 2006; Paardekooper 2014).

4.3. Planetary Migration

It is then easy to estimate the planetary migration timescale. Using some typical parameters, Tanaka et al. (2002) found it would be typically 10^6 yr with inward migration, which is comparable to or shorter than the lifetime of PPDs. Tanaka et al. (2002) give the (outward) migration timescale

$$\tau_{\mathrm{mig}} = \frac{L_p}{2\Gamma}, \tag{29}$$

where L_p is the angular momentum of the planet $M_p(GM_\star r_p)^{1/2}$. With $f_d = 0.01$, Figure 5 allows Γ ranges from $-3 h_p\Gamma_0$ to $30 h_p\Gamma_0$. Using the same parameters as those used in Tanaka et al. (2002), the final result would be -10^6 to 10^5 yr (the negative sign means inward migration), depending on τ. This illustrates how the ST can dominate both the CT and LT, consequently driving outward planetary migration.

6

5. Discussions and Conclusions

In this paper, we explore planetary migration in dust–gas coupled PPDs. Employing linear calculations with NSH equilibrium under the shearing sheet approximation, we unveil the significant contribution of the dusty quasi-drift mode to planetary migration.

In such two-fluid systems, the quasi-drift mode emerges and governs the wavy behaviors in close proximity to planets. As the dust fraction increases, the amplitude of dusty quasi-density waves grows, while the quasi-drift modes are damped rapidly. Consequently, quasi-density waves, unable to propagate within the corotation region, take precedence in regions farther from the planet. The quasi-drift mode features an extremely short radial wavelength, with a dispersion relation of $\tilde{\omega} = f_g \, \boldsymbol{W}_s \cdot \boldsymbol{k}$, indicating its subsonic nature originating from dust drift.

The quasi-drift mode engenders a wake characterized by a short radial length scale, positioned ahead of the planet, yielding a positive torque, referred to as the ST. Additionally, the NSH velocity alters both LT and CT, with LR points undergoing a shift due to sub-Keplerian rotation and CT experiencing amplification from radial velocity.

For a typical dust fraction (~ 0.01), the final outcome of planetary migration depends on the degree of coupling between dust and gas, quantified by the dimensionless stopping time τ. We find that at low τ values, both dust and gas contribute negative torque, resulting in inward migration. Conversely, when τ approaches unity, both dusty and gaseous torques peak. Notably, the dominance of dusty ST, originating from the quasi-drift mode, drives a rapid outward migration with characteristic timescales of 10^5 yr, which can solve the existing puzzle that planets migrate inward fast. We also conduct a tentative survey for the torques with different f_d. Near $f_d = 0.01$, we find the absolute ST value increases with higher f_d. This means planetary migration will be faster with a higher f_d. At the moment, nonlinear effects and other physical ingredients, like planetesimal formation, might be important. Then, the ST calculations with higher f_d should be calculated with more considerations.

An essential concern is the softening length, with a value of $1/8$ utilized in this work, as validated in Dong et al. (2011). Furthermore, the consistency of gaseous torques with Tanaka et al. (2002) is crucial for the quantitative calculation of ST. We notice that the quasi-drift mode is excited near the planet and sensitive to planetary potential, which means it must be careful with the use of softening length.

Our findings are consistent with Benítez-Llambay & Pessah (2018), who conducted hydrodynamic simulations for dust–gas PPDs. They found that when τ is low, dusty torque is negative, while at higher τ values, a dusty cavity behind the planet results in a large positive torque. Radial short-wavelength structures inside the planet of dust also appear in their simulations as their Figures 1 and 4 show, which imply the nonlinear phase of our calculations.

Exploring the vast parameter space, including the dust mass fraction and aspect ratio, is crucial. While standard PPDs are presumed to have $f_d \sim 0.01$, recent findings by Stefánsson et al. (2023) suggest this could be underestimated, possibly reaching about 0.10. We also do not consider an Epstein regime, unlike Hopkins & Squire (2018), allowing a variation for stopping time. However, there is no fundamental physical difference between them, and ST still works. In this work, we assume the PPD as a thin disk and use vertically integrated equations, which are used widely for the investigation of planetary migration (e.g., Goldreich & Tremaine 1980; Korycansky & Pollack 1993). However, the effects of vertical structure on ST deserve future identification (Tanaka et al. 2002; Tanaka & Okada 2024). Other details and more physical ingredients, such as dust diffusion and accretion, also warrant further investigation. Dust diffusion tends to restrain the waves with short scale, which means it might weaken the effect of ST, similar to the stabilization of streaming instability (Chen & Lin 2020; Umurhan et al. 2020). It has been found that gas accretion contributes a lot to planetary migration (Laune et al. 2024; Li et al. 2024). For a low-mass planet, dust accretion might affect the ST through changing the drift velocities nearby. We will investigate both of them in the future.

In conclusion, the relative motion of dust and gas facilitates the existence of the dusty drift mode, resulting in ST and altering the migration history of low-mass protoplanets in the early phase. Depending on the coupling between dust and gas, outward migration becomes a viable scenario.

ORCID iDs

Qiang Hou ⓘ https://orcid.org/0000-0002-8125-7320
Cong Yu ⓘ https://orcid.org/0000-0003-0454-7890

References

Balbus, S. A. 2003, ARA&A, 41, 555
Baruteau, C., Fromang, S., Nelson, R. P., & Masset, F. 2011, A&A, 533, A84
Baruteau, C., & Masset, F. 2008, ApJ, 672, 1054
Benítez-Llambay, P., Masset, F., Koenigsberger, G., & Szulágyi, J. 2015, Natur, 520, 63
Benítez-Llambay, P., & Pessah, M. E. 2018, ApJL, 855, L28
Chen, K., & Lin, M.-K. 2020, ApJ, 891, 132
D'Angelo, G., & Lubow, S. H. 2010, ApJ, 724, 730
Dong, R., Rafikov, R. R., & Stone, J. M. 2011, ApJ, 741, 57
Goldreich, P., & Lynden-Bell, D. 1965, MNRAS, 130, 125
Goldreich, P., & Tremaine, S. 1979, ApJ, 233, 857
Goldreich, P., & Tremaine, S. 1980, ApJ, 241, 425
Guilera, O. M., Benitez-Llambay, P., Miller Bertolami, M. M., & Pessah, M. E. 2023, ApJ, 953, 97
Hopkins, P. F., & Squire, J. 2018, MNRAS, 480, 2813
Hsieh, H.-F., & Lin, M.-K. 2020, MNRAS, 497, 2425
Huang, S., & Yu, C. 2022, MNRAS, 514, 1733
Kanagawa, K. D. 2019, ApJL, 879, L19
Kley, W., & Nelson, R. P. 2012, ARA&A, 50, 211
Korycansky, D. G., & Pollack, J. B. 1993, Icar, 102, 150
Laune, J., Li, R., & Lai, D. 2024, arXiv:2405.00296
Li, H., Finn, J. M., Lovelace, R. V. E., & Colgate, S. A. 2000, ApJ, 533, 1023
Li, Y.-P., Chen, Y.-X., & Lin, D. N. C. 2024, ApJ, 971, 130
Masset, F. S., & Papaloizou, J. C. B. 2003, ApJ, 588, 494

Miranda, R., & Rafikov, R. R. 2020, ApJ, 892, 65
Nakagawa, Y., Sekiya, M., & Hayashi, C. 1986, Icar, 67, 375
Narayan, R., Goldreich, P., & Goodman, J. 1987, MNRAS, 228, 1
Ogilvie, G. I., & Lubow, S. H. 2006, MNRAS, 370, 784
Paardekooper, S., Dong, R., Duffell, P., et al. 2023, in ASP Conf. Ser. 534, Protostars and Planets VII, ed. S. Inutsuka et al. (San Francisco, CA: ASP), 685
Paardekooper, S. J. 2014, MNRAS, 444, 2031
Pan, L., & Yu, C. 2020, ApJ, 898, 7
Pierens, A., & Huré, J. M. 2005, A&A, 433, L37
Press, W. H., Teukolsky, S. A., Vetterling, W. T., & Flannery, B. P. 1992, Numerical Recipes in FORTRAN. The Art of Scientific Computing (Cambridge: Cambridge Univ. Press)
Rafikov, R. R., & Petrovich, C. 2012, ApJ, 747, 24

Squire, J., & Hopkins, P. F. 2018a, ApJL, 856, L15
Squire, J., & Hopkins, P. F. 2018b, MNRAS, 477, 5011
Stefánsson, G., Mahadevan, S., Miguel, Y., et al. 2023, Sci, 382, 1031
Tanaka, H., & Okada, K. 2024, ApJ, 968, 28
Tanaka, H., Takeuchi, T., & Ward, W. R. 2002, ApJ, 565, 1257
Terquem, C. E. J. M. L. J. 2003, MNRAS, 341, 1157
Umurhan, O. M., Estrada, P. R., & Cuzzi, J. N. 2020, ApJ, 895, 4
Ward, W. R. 1986, Icar, 67, 164
Ward, W. R. 1997, Icar, 126, 261
Wu, Y., Chen, Y.-X., & Lin, D. N. C. 2024, MNRAS, 528, L127
Youdin, A. N., & Goodman, J. 2005, ApJ, 620, 459
Yu, C., Li, H., Li, S., Lubow, S. H., & Lin, D. N. C. 2010, ApJ, 712, 198
Ziampras, A., Nelson, R. P., & Paardekooper, S.-J. 2024, MNRAS, 528, 6130